CrystEngComm

Accepted Manuscript

ROYAL SOCIETY OF CHEMISTRY

www.rsc.org/crystengcomm

Mild synthesis of {001} facets predominated Bi$_2$O$_2$CO$_3$ clusters with outstanding simulated sunlight photocatalytic activities

Li-Min Yang, Guo-Ying Zhang*, Hai-Rong Wang, Xue Bai, Xing-Qi Shen, Jing-Wang Liu, Dong-Zhao Gao

Tianjin Key Laboratory of Structure and Performance for Functional Molecules; Key Laboratory of Inorganic-Organic Hybrid Functional Material Chemistry, Ministry of Education; College of Chemistry, Tianjin Normal University, Tianjin 300387, China

* Corresponding author. Tel./Fax: +86 22 23766532

E-mail address: hxxyzgy@mail.tjnu.edu.cn (G.-Y. Zhang)

Abstract: $Bi_2O_2CO_3$ clusters built up of ultrathin nanosheets with predominated {001} facets were facilely synthesized *via* a template-free hydrothermal strategy at a mild temperature of 60 °C. The Na_2CO_3 dosage and reaction temperature are confirmed to be key parameters to obtain the hydrolysis product of $(Bi_2O_2)^{2+}$ from bismuth nitrate and provide suitable microenvironment for the assembly of nanosheets. The sample exhibits obviously improved photocatalytic activity for the degradation and mineralization of Rhodamine B compared with thicker $Bi_2O_2CO_3$ plates of less exposed {001} planes, with the reaction rate constant *k* enhanced by 3.4 folds. Results of photoluminescence and electrochemical impedance confirm that the {001} facets are reactive and favorable for the separation and migration of photogenerated carriers, which primarily accounts for the superior photocatalytic behavior of $Bi_2O_2CO_3$ clusters. In addition, the enhanced specific surface area should also contribute to the improved photocatalytic activity. Based on the band edge positions of $Bi_2O_2CO_3$ and the redox potentials of detected oxidative species, a possible migration mechanism of photogenerated e^-/h^+ pairs on the surface of $Bi_2O_2CO_3$ is proposed. This work provides some new insights for the rational design and synthesis of facet-dependent semiconductor photocatalyst under mild conditions.

Keywords: Mild synthesis; Template-free; $Bi_2O_2CO_3$; Active facets; Photocatalysis; Carrier migration

1. Introduction

Environmental problems related to harmful organic pollutants in water bring severe threats to sustainable development of human in modern society. Semiconductor-based photocatalysis is considered to be an attractive and promising strategy for water remediation due to the utilization of solar energy and environmental friendliness.[1,2] Since the photoelectrochemical water splitting over a TiO_2 electrode was reported in 1972,[3] much attention has been paid to the development of highly efficient semiconductor photocatalysts. Up to now, a variety of active photocatalysts including metal oxides, sulfides, oxynitrides, as well as the metal-free semiconductors have already been developed.[4-7]

Among various semiconductors, the bismuth-containing materials with admirable photocatalytic properties for the degradation of organic pollutants have attracted much attention in the photocatalytic field such as Bi_2O_3,[8] Bi_2WO_6,[9] Bi_2MoO_6,[10] $BiVO_4$,[11] BiOX (X=Cl, Br, I),[12-15] $Bi_4B_2O_9$,[16] *etc*. Bi-based carbonate $Bi_2O_2CO_3$ (BOC) is another member of the bismuth compounds with typical Sillén-phase structure in which Bi-O layers and CO_3^{2-} layers are orthogonally intergrown with each other.[17] Though previous application of BOC were only restricted to medicine and microelectrode,[18,19] it has recently joined the photocatalytic family because of the characteristic of indirect gap semiconductor[20] as well as the ability to accelerate the separation of electron-hole (e^-/h^+) pairs due to the particular layered structure.[21] Since the early research of BOC as photocatalyst for degradation of dye under UV illumination,[22] much efforts have been devoted to obtain BOC with reduced band

gap,[23] decreased particle size and large specific surface area[24,25] to improve the photocatalytic activity.

The photocatalytic behavior of a photocatalyst is affected not only by the inherent nature including band gap, size, and dispersity, but also by the surface state involving electric charge, absorption properties, defects, and so on. In particular, the exposed crystal surface has been confirmed to be another key factor to influence the photocatalytic activity.[26] The photocatalytic reaction occurs at the interface of the reactant and catalyst, so photocatalytic activity is strongly dependent on the surface microstructure and exposed facets.[27] Pioneering works on the research of TiO_2[28,29] and BiOCl[30,31] with highly reactive facets have paved a new way for the enhancement of photocatalytic performance. Our group and Huang *et al.* have recently reported the superior photocatalyst of $Bi_6O_6(OH)_3(NO_3)_3 \cdot 1.5H_2O$ with predominated {110} facets[32] and $Bi_2O_2(OH)(NO_3)$ with active {001} facets,[33] respectively. By far, a few works has been carried out to investigate the reactive crystal facets of BOC photocatalyst. Xie *et al.*[34] first put forward BOC photocatalyst from viewpoint of structural understanding. They proposed that BOC with controlled {001} plane showed excellent photocatalytic activity due to the large distortion of Bi-O polyhedron and easily derived oxygen defects on the exposed facets. Huang and coauthor's work[35] further confirmed the {001} facets dependent BOC structure by dye degradation. However, the above mentioned BOC samples were exclusively achieved through hydrothermal process at a high temperature of 180-200°C and in a long span of 24 h with the assistance of citric acid or urea. Yin's group[36] reported an ambient

route to prepare BOC flowers but with anisotropic growth along {110} planes, in which the surfactant CTAB is needed to achieve the morphology control. BOC nanosheets with exposed {001} facets were also obtained *via* an ambient conversion of Bi_2O_3 with atmospheric CO_2. But the heterogenerous reaction is much slow and it has to take a prolonged time of 24 h to complete the synthesis. Furthermore, residual intermediate phase of $(BiO)_4CO_3(OH)_2$ coexist in the final BOC sample due to low atmospheric CO_2 pressure.[37] Apparently, the majority of hitherto reported synthetic routes of BOC structures with special exposed facets are either time- and energy-consumption, or they rely on morphology control agent, which would make the scale-up synthesis more sophisticated. It is therefore attractive to develop a more facile, economic and effective strategy to prepare {001} facets exposed BOC structures. And it is necessary to systematically explore the key preparation parameter and clarify the relationship between structure and photocatalytic performance.

In the work, we have successfully synthesized {001} facets predominated BOC clusters *via* a template-free hydrothermal route at a mild temperature of 60 °C for a short time of 4 h. Parameter control experiments indicate that Na_2CO_3 dosage and reaction temperature are vital factors to achieve {001} facets preferred BOC structures. The BOC clusters exhibit obviously superior photocatalytic activity towards dye degradation than less {001} facets exposed BOC plates with the rate constant *k* enhanced by 3.4 folds. The active oxidation species are ascertained using scavenger experiments and electron spin resonance techniques. Combining the band edge of BOC and the redox potentials of the active species, a possible migration

mechanism of photogenerated e^-/h^+ pairs on the BOC surface is proposed.

2. Experimental section

Preparation

All the reagents were of analytical grade and used as received without further purification. BOC clusters with preferred {001} facets were prepared as follows: 1.0 mmol of $Bi(NO_3)_3 \cdot 5H_2O$ was dissolved in 17.0 mL of distilled water, into which 6.0 mmol of Na_2CO_3 was introduced under fiercely stirring. After constantly stirring for another 30 min, the resulting suspension was transferred into a 25 mL Teflon-lined stainless steel autoclave and heated at 60 °C for 4 h. After the autoclave cooled to room temperature naturally, the solid products were collected by centrifugation, washed with deionized water and absolute ethanol for several times, and then dried at 60 °C in air. The temperature series samples were treated at a temperature between ambient to 140 °C for 4 h, and Na_2CO_3 dosage series samples were prepared at 60 °C for 4 h, keeping the other conditions unchanged. (Table S1)

Characterization

The crystal phase and composition of the samples were characterized by X-ray diffraction (XRD) on a Bruker D8-Advance diffractometer with Cu Kα radiation. X-ray photoelectron spectroscopy (XPS) images were recorded on a Thermo Fisher K-alpha X-ray photoelectron spectrometer. Morphologies and microstructures of the prepared products were examined with a field-emission scanning electron microscopy (FEI, NOVA Nano SEM 230) and a high-resolution transmission electron microscopy (FEI, Tecnai G^2 F20). N_2 sorption isotherms were collected at liquid nitrogen

temperature using a Micromeritics ASAP2020 surface area and porosity analyzer. Diffuse reflectance spectra (DRS) were recorded on a JASCO V-550/V-570 UV-vis spectrophotometer fitted with an integrating sphere accessory. The photoluminescence (PL) spectra were recorded with an F-4500 fluorescence spectrophotometer. Total organic carbon (TOC) was measured by an Elementarvario TOC analyzer. The electron spin resonance (ESR) measurements were performed on a JEOL JES-FA200 ESR spectrometer with a xenon lamp as the simulated sunlight source. The DMPO (5,5′-dimethyl-1-pirroline-N-oxide) was employed as a spin-trap reagent to trap the active species of hydroxyl (•OH) and superoxide radicals ($O_2^{-}\cdot$) in aqueous and methanol dispersions, respectively.

Photoelectrochemical measurement

The electrochemical impedance spectroscopy (EIS) was conducted using a Versa START4-200 electrochemical work station and operated in a standard three-electrode configuration system with a working electrode, a Pt counter electrode, and an Ag/AgCl reference electrode. The working electrode was prepared by drop-casting 0.5 mL of the photocatalyst sample dispersed in N,N-Dimethylformamide (DMF) solution (6.0 mg mL^{-1}) onto an indium tin oxide (ITO) glass of (1cm × 2 cm) and then dried at 60 °C in vacuum for 1 h. The electrolyte was 2.5 mmol L^{-1} $K_3[Fe(CN)_6]$-$K_4[Fe(CN)_6]$ (1:1) containing 0.1 mol L^{-1} KCl aqueous solution. A 300 W Xe lamp was employed for the simulated light irradiation.

Photocatalytic degradation experiments

Photocatalytic activities of the samples were evaluated for the degradation and

mineralization of RhB solution under simulated sunlight with a 250 W Xe lamp in a photoreactor equipped with water circulation facility. In each test, 5.0 mg of photocatalyst was added into RhB solution with the initial concentration of 10^{-5} M in a quartz tube. Before illumination, the suspension was magnetically stirred in dark for 30 min to establish an adsorption-desorption equilibrium. Then at given time intervals, one quartz tube was taken out and the photocatalyst was immediately separated by centrifugation to analyze the supernate by a Shimadzu 2550 UV-vis spectrophotometer. Photocatalytic degradation to methylene blue (MB), crystal violet (CV) and methyl orange (MO) were followed the same procedure.

3. Results and discussions

3.1 Phase and composition analysis

The phase and purity of the sample synthesized at 60 °C for 4 h were determined by XRD, and the typical diffraction pattern is shown in Fig. 1. All of the diffraction peaks could be readily indexed to the tetragonal BOC ($a = b = 3.865$ Å, $c = 13.675$ Å, JCPDS: 41-1488). No other impurity peaks from $BiO(NO_3)$, $Bi_6O_6(OH)_3(NO_3)_3$ and other bismuth hydrolysis product were detected, indicating the high purity of the product. The sharp and strong diffraction peaks demonstrate the high crystallinity of BOC. But it is noteworthy that the (002) peak belonging to {001} facets is obviously strengthened compared with the standard values. The intensity ratio of the (002) peak to the strongest (013) peak in the as-obtained BOC sample is calculated to be 0.54, increased by *ca.* 2.2 folds compared with the standard value of 0.25. The XRD result may imply the preferential growth of a specific crystal plane in BOC.

The elemental composition and chemical states of the BOC photocatalyst were analyzed by XPS. The typical survey spectra in Fig. 2a display three elements of Bi, O and C contained in the sample. Fig. 2b displays two strong symmetrical characteristic spin-orbit splitting of Bi^{3+} 4f peaks at 159.5 and 164.8 eV, which are assigned to Bi $4f_{7/2}$ and Bi $4f_{5/2}$, respectively.[38] The XPS peak for C 1s (Fig. 2c) located at 284.8 eV is ascribed to the adventitious hydrocarbon from the XPS instrument,[39] while the peak at 288.7 eV can be assigned to the carbonate ion in the as-prepared BOC sample.[40] Besides the typical signals of Bi^{3+} and C, the broad and asymmetry peak at ~531 eV indicates the complicated oxygen species. As given in the fitted O1s spectrum (Fig. 2d), the peak at 530.3 eV is characteristic of Bi-O binding energy in BOC^{41} and the other two peaks at 531.2 and 532.1 eV can be ascribed to carbonate species and adsorbed H_2O (or surface hydroxyl groups) on the surface.[42] The XPS result further demonstrates the high purity of BOC, in good consistence with XRD analysis.

3.2 Morphology and microstructure

The morphology and microstructure of BOC were identified using SEM and TEM. The overall SEM image in Fig. 3a indicates that the sample consists of clusters with diameter ranging from 1.2 to 1.6 μm, which are constructed by irregular nanosheets. The close-up view in inset shows that the nanosheets are interlaced and present lateral size of 100-300 nm and thickness of ca. 5-15 nm. The TEM image in Fig. 3b shows quasi-elliptic outline with jigsaw puzzle analogues inter-connected, in accordance with SEM results. The loose construction of the nanosheets leaves lots of mesopores

in the cluster, which may serve as transport tunnels for dye molecules and active species to improve the physicochemical activities. The HRTEM image (Fig. 3c) of one nanosheet shows clear lattice fringes with interplanar space of 0.273 nm, which can be indexed into the {110} crystal planes and implies the high crystallinity. The single-crystalline nature of BOC is further confirmed by the well-ordered dot pattern of selected-area electron diffraction (SAED) in Fig. 3d. The measured value of indicated angle is 45° and corresponds to the theoretical calculation between the {200} and {110} facets. The SAED pattern is assigned to the [001] zone-axis diffraction spots of BOC. The above analyses demonstrate that the top and bottom exposing surfaces belong to {001} facets with schematic illustration in Fig. 3e. The TEM data and XRD results together confirm the oriented {001} exposed crystal planes of BOC.

3.3 Effect of preparation parameters

To give a better understanding of the key parameter on the formation of BOC clusters, control experiments of Na_2CO_3 dosages were conducted. As shown in Fig. 4a, when stoichiometric 0.5 mmol Na_2CO_3 in $Bi_2O_2CO_3$ formula is employed, the sample is scattered microrods with length of 10-25 μm and width of 1-3 μm. The corresponding XRD pattern is indexed to $Bi_{12}(OH)_6O_{10}(NO_3)_6(NO_3)_4(H_2O)_6$ (BON, JCPDS No. 76-5376), a complex hydrolysis product of $Bi(NO_3)_3$. With the Na_2CO_3 dosage increasing to 1.0 mmol, some nanoflakes emerge among the microrods (Fig. 4b) and the product is a mixture of BON and BOC. When Na_2CO_3 amount is further ascended to 2.0 mmol, the microrods disappear completely and the sample consists of isolated plates with lateral sizes of 0.3-1.2 μm and thickness of 30-60 nm. At this

stage, the XRD pattern has been indexed to pure BOC but with low crystallinity and un-obvious oriented (002) peak. In the presence of 4.0 mmol of Na_2CO_3, BOC aggregates stacked of smaller and thinner nanosheets are produced. Finally, well-defined fluffy BOC clusters are assembled by nanosheets with average thickness *ca.* 10 nm when 6.0 mmol of Na_2CO_3 is used. In addition, one can see that the intensity of (002) peak increases gradually with enhanced Na_2CO_3 dosage. A vivid calculation shows that the intensity ratio of (002)/(013) is 0.38, 0.51 and 0.54 for Na_2CO_3 amount of 2.0, 4.0 and 6.0 mmol, respectively. However, the sample obtained with superabundant Na_2CO_3 of 10.0 mmol (Fig. S1) shows dominant thicker plates with decreased intensity ratio of (002)/(013) to 0.48.

Based on above analysis, the phase and morphology of hydrothermal product depend greatly on the Na_2CO_3 amount. The reagent Na_2CO_3 is believed to play triple roles in the preparation of BOC clusters. Firstly, it acts as one reactant to provide CO_3^{2-} for $Bi_2O_2CO_3$. Secondly, it can offer a suitable medium pH for Bi^{3+} to get the hydrolysis product of $(Bi_2O_2)^{2+}$, another reactant for BOC. It is known that the hydrolysis product of Bi^{3+} is complex and involves $BiO(NO_3)$, $Bi(OH)_2NO_3$, $Bi_2O_2(OH)NO_3$ and other more complicated compositions, which is significantly affected by the medium acidity.[43] As shown in Fig. 4f, the strong acidic medium of pH < 3.1 (Table S2) in the presence of less than 1.0 mmol Na_2CO_3 would induce BON, one complex hydrolysis product of Bi^{3+}. Pure BOC is obtained with at least 2.0 mmol Na_2CO_3 used, when the medium pH is greater than 6.0 (Table S2). It illustrates that a weak acidic or alkaline medium created by Na_2CO_3 is required to neutralize the strong

hydrolysis of Bi^{3+}. Thirdly, enough Na_2CO_3 of 6.0 mmol provides a suitable alkaline medium of pH 9.4 for the construction of BOC nanosheets into clusters.

To verify the proposed roles of Na_2CO_3, the extended experiments of $(NH_4)_2CO_3$, Li_2CO_3 and K_2CO_3 were performed. As shown in Fig. S2-S4, the products exhibit a similar morphology evolution from microrods to plates till to clusters with increased amount of carbonate, accompanied by phase change from BON to BOC. A vivid comparison of the relationship of all carbonate dosage with medium pH and product phase is given in Table S2. It can be seen that the strong acidic medium of pH < 2 with usage of 0.5 mmol carbonate exclusively produce BON. When the medium pH exceeds 5 with at least 2.0 mmol carbonate used, pure BOC phase is obtained in all cases. The sole difference is that in the presence of 1.0 mmol $(NH_4)_2CO_3$ and Li_2CO_3 (pH < 3), the product is still BON in compared with the cases of Na_2CO_3 and K_2CO_3, in which a mixed phase of BON and BOC is obtained. It is ascribed to the different alkaline of the carbonates in a sequence of $(NH_4)_2CO_3$ < Li_2CO_3 < Na_2CO_3 < K_2CO_3 as illustrated by the medium pH gradient. Thus the important role of carbonate is to provide suitable medium pH for the formation of pure BOC phase. Another common point is that fluffy BOC clusters become assembled at a suitable medium pH up to ca. 9.0 when 6.0 mmol carbonate is used. The detailed intensity ratio of (002)/(113) is all increased from 2.0-6.0 mmol with the maximum at 6.0 mmol carbonate used (Table S3). The product phase, microstructure and morphology with different carbonates give basically similar results, strongly validating the key actions of CO_3^{2-} in the synthesis of BOC clusters.

12

The hydrothermal temperature is another crucial factor to achieve {001} facets predominated BOC structures. As shown in Fig 5a, BOC sheets with lateral sizes of 50-300 nm and thickness of 25-50 nm can be synthesized at ambient but with weak crystallization. The sheets get thinner to ca. 20 nm at increasing temperature of 40 °C (Fig. 5b) and well-defined BOC clusters built up of nanosheets with thickness of 5-15 nm are obtained at 60 °C (Fig 5c). At a higher temperature of 100 °C, the BOC clusters disappear completely and are replaced by thicker nanosheets of 20-40 nm. Further increasing the temperature to 140 °C, the product has grown into plates with much more thickness of 40-70 nm. Combined with previous TEM analysis, the thick plates have reduced {001} exposing facets, which is further confirmed by the XRD results. As shown in Fig. 5f, all the XRD patterns can be ascribed to pure BOC but with increasing diffraction intensity from RT to 140 °C. Detailed comparison shows that the intensity ratios of (002)/(013) are 0.39, 0.54, 0.48 and 0.32 at 40 °C, 60 °C, 100 °C and 140 °C, respectively. Obviously, the BOC clusters prepared at 60°C exhibits the most percentage of {001} facets.

3.4 Porosity and optical property

BOC clusters, thinner and thicker nanoplates prepared at obtained at 60 °C, 40 °C and 140°C are selected to investigate the porosity and optical property. As shown in Fig. 6a, the samples all exhibit type IV isotherms (BDDT classification) with type H3 hysteresis loops, indicating the mesoporous nature.[44] But the maximum adsorption quantity of BOC-60°C reaches up to 45.3 m^3 g^{-1}, which is increased by 1.5 and 5.1 folds compared with that of BOC-40°C (29.9 m^3 g^{-1}) and BOC-140°C (8.9 m^3 g^{-1}),

respectively. The result is well interpreted by the higher BET surface area of 16.2 m^2 g^{-1} for BOC clusters than that of 13.9 m^2 g^{-1} and 5.1 m^2 g^{-1} for thinner and thicker BOC nanoplates, respectively. Although the BJH pore-size distribution plots display similar mesopore sizes in 2.0-4.5 nm, BOC-60°C and BOC-40°C exhibits obviously larger dv/dw value than thicker BOC-140°C plates. The BOC clusters with improved surface area and porosity exhibit a slightly increased adsorption for RhB molecules (Table S4). It suggests that the sample could provide a little more reactive sites and transport paths for reactants and active species in the photocatalysis.[45] The optical absorption properties of BOC samples were studied by UV-vis DRS spectra with results shown in Fig. 6b. The samples present semiconductor characteristic with an absorption threshold of *ca.* 379 nm and the BOC-60°C and BOC-40°C exhibits slightly higher absorption intensity. Band gap of BOC samples was determined by optical absorption near the band edge by the following equation $\alpha h v = A(h v - E_g)^{n/2}$, where α, $h v$, A, and E_g are absorption coefficient, photonic energy, proportionality constant, and band gap, respectively.[46] In the equation, n decides the type of the transition in a semiconductor ($n = 1$, direct absorption; $n = 4$, indirect absorption). The clear linearity of $(\alpha h v)^{1/2}$ *vs.* $h v$ in the inset indicates the indirect transition of BOC with $n = 4$, which is consistent with the previous literature.[20] By extrapolating the tangent to the *x*-axis in the plot, E_g of the BOC samples obtained at 60°C, 40°C and 140°C is estimated to be 3.23 eV, 3.24 eV and 3.27 eV, respectively. The slightly increased absorption and decreased E_g of BOC-60°C may be due to multiple reflections of the porous structure and increased inner stress in ultrathin BOC

14

nanosheets, which should benefit for the light usage in photocatalysis.

3.5 Photocatalytic properties

The photocatalytic degradations of RhB over Na_2CO_3 dosage and temperature series samples were evaluated under simulated sunlight irradiation with the results given in Fig.7. Contrast experiments show that the RhB photolysis in the absence of photocatalyst and the dye adsorption in the dark can both be ignored. The variations of Na_2CO_3 dosage and reaction temperature have great influences on degradation efficiencies. The BOC clusters prepared at 60 °C with 6.0 mmol of Na_2CO_3 exhibit the best photocatalytic activity with 97.9% removal of RhB in 80 min, and the calculated pseudo first-order kinetics constant k is 0.04626 min^{-1}. The samples with Na_2CO_3 usage of 0.5 and 1.0 mmol give a rather low photocatalytic activity (Fig. 7a-b) due to the incomplete formation of BOC phase as indicated in Fig. 4. Pure BOC plates with Na_2CO_3 dosage of 2.0 mmol begin to show obviously improved photocatalytic activity but still have a weak rate constant k of 0.01657 min^{-1}, which is only 0.36 compared with that of BOC clusters. Then the degradation efficiency is continuously enhanced with increasing Na_2CO_3 dosage and reaches the maximum at 6.0 mmol. However, excess Na_2CO_3 of 10.0 mmol results a reversely decreased photocatalytic activity. As previous analysis in Fig. 4, the BOC clusters with Na_2CO_3 dosage of 6.0 mmol have the most exposed {001} facets, which is believed to play a vital role as reactive crystal planes. The assumption is further supported by the photocatalytic results over BOC samples of temperature series. As indicated in Fig. 7c-d, the degradation of RhB increases at first and then decreases with elevated temperature,

and the best activity is achieved at 60 °C. The rate constant k for BOC-60°C is as

much as 3.4 times compared with that of the BOC-140°C sample. Above SEM and

XRD analyses in Fig. 5 show that BOC samples obtained at higher temperature have

thickened sheets and lowered (002) diffraction ratio, which corresponds to decreased

{001} exposing planes. Accordingly, the relationship between structure and property

strongly confirm the formation of {001} reactive facets prevailed BOC structure *via*

the mild hydrothermal strategy.

To give more vivid comparison, temporal evolutions of RhB spectral change over

BOC-60°C and BOC-140°C were recorded. As shown in Fig. 8a, the absorption peak

of RhB quickly diminishes with prolonged irradiation over BOC-60°C, accompanied

by a blue-shift of the main peak from 553 nm to 534 nm after 60 min illumination,

and the complete discoloration of RhB is achieved in 80 min. It is known that the

degradation mechanism of RhB usually passes through two different pathways: the

photosensitized N-de-ethylation and photocatalytic destruction of chromophore

structure. And the absorption peak of the gradually de-ethylated RhB would shift

from the initial 553 nm to the final 498 nm with 70% of molar absorptivity

maintained.[47] The rapid decline of RhB absorption to 11% in 60 min and the slight

blue-shift of the absorption peak to 534 nm indicate that it is the photocatalysis rather

than photosensitization that predominates the degradation process of RhB. In

comparison, the degradation speed is greatly reduced in the presence of BOC-140°C

sample (Fig. 8b). No obvious blue-shift of the absorption peak occurs and there is still

34.5% of the RhB molecules left after 80 min irradiation. The higher TOC

mineralization efficiency of RhB solution over BOC-60°C (Fig.S5) further confirms

the improved photocatalytic activity of BOC clusters with reactive {001} facets and

larger surface area. The investigation of photocatalytic performance was also

extended to other dyes including CV, MB and MO (Fig. 8c). The BOC-60°C exhibit

generally enhanced photocatalytic activity for removal of different dyes compared

with BOC-140°C, convincingly displaying the superior structure of BOC clusters.

The circulating runs of the photocatalytic degradation of RhB were carried out to

evaluate the recoverability and stability of BOC clusters. The photocatalyst is easily

recycled due to the micrometer size of the hierarchical structure. Following simple

washing and drying steps, the recovered photocatalyst can be reused. As indicated in

Fig. 8d, the photocatalytic activity of BOC clusters does not exhibit any obvious loss

after five recycles for the degradation of RhB. The XRD results of BOC samples

collected after the 3th and 5th runs maintain preferential (002) planes with (002)/(013)

ratio of 0.53 and 0.51, respectively (Fig. S6). It implies that the BOC clusters are of

high stability and not easy to be photocorroded during the photocatalysis, which is

significant for practical applications in environmental remediation.

3.6 Photocatalytic mechanism

PL emission of a photocatalyst comes from the recombination of free carriers and

can be used to disclose the separation and migration of photogenerated e^-/h^+ pairs.

The lower PL intensity often indicates a decreased recombination rate of carriers and

thus an improved photocatalytic activity.[48] Fig. 9a shows the typical PL spectra of

BOC-40°C, 60°C and 140°C excited at 300 nm, respectively. Although the samples

exhibit similar broad emission in 340-550 nm with the main peak at 394 nm, BOC-60°C with the most preferential {001} facets gives the weakest PL intensity. It indicates that the photogenerated carriers in BOC clusters are more effectively separated and transferred. EIS is another forceful technique to study the migration ability and interface reaction ability of the electrons in a photocatalytic material. The electrode generally exhibits a semicircle over the high frequency range, followed by a linear part in the low frequency range. And little arc radius on the EIS Nyquist plot reveals increased charge mobility in the semiconductor material and promoted reaction rate of the photogenerated carriers on the interface between electrolyte and the semiconductor.[49] As the results show in Fig. 9b, the impedance arc radius of BOC-60°C is obviously the minimum compared with that of BOC-40°C and 140°C. The EIS data were fitted with the equivalent circuit model in inset. Here, the R_1 and Z_w represent the resistance of the solution and Warburg impedance, while the R_2 and C are charge transfer resistance and surface capacitance of BOC films, respectively. It is found that the R_2 value corresponding to the semicircle diameter of BOC-60 °C (83.2 Ω) is significantly smaller than those of the BOC-40 °C (150.2 Ω) and BOC-140 °C (185.0 Ω), suggesting a higher charge mobility and interface reaction in BOC clusters. **According to the literatue,**[34] on the exposed {001} plane of BOC, the Bi-O [8]-coordination unit compressed along the c-axis would supply lots of oxygen defects from the unstable oxygen which have the longest bond with Bi atom. In addition, the thinness BOC sheet induces an internal electric field duo to large distortion of Bi-O polyhedron. The factors can both facilitate the separation and

migration of photogenerated e^-/h^+ pairs in the crystal, and thus boost the subsequent photocatalytic reaction.

To investigate the reactive oxidation species in the photocatalytic process of BOC clusters, trapping experiments were performed by adding individual scavengers to the RhB/BOC system. In this study, different chemicals including ethylene diamine tetraacetic acid (EDTA, a hole scavenger), *tert*-butanol (TBA, a $\cdot$OH scavenger), *p*-benzoquinone (BQ, a $O_2^-\cdot$ scavenger),[50,51] and continuous N_2-sparging were employed. The trace introduction of EDTA, TBA and BQ brings slight pH change from the initial 4.80 to 4.64, 4.91 and 5.07, respectively. The little pH variation has no obvious influence to the photocatalytic activity as indicated in Figure S7. The results in Fig. 10a show that the introduction of 1.0 mM EDTA leads to a remarkable inhibition for the degradation efficiency of RhB from 97.9% to 28% after 80 min irradiation. It indicates the most importance of direct oxidation by holes in the photocatalytic process. The presence of 1.0 mM BQ also causes fast deactivation of BOC clusters with degradation efficiency decreased by 37.6% in 80 min. It should be due to the capture of irradiated $O_2^-\cdot$ by BQ and the decrease in the amount of active $O_2^-\cdot$ for photocatalytic reaction. The vital roles of h^+ and $O_2^-\cdot$ can be further confirmed by the photocatalytic process with continuous N_2-sparging, in which the degradation of RhB is significantly suppressed. It is known that the presence of oxygen is important and it can act as an efficient e^- trap, leading to the generation of $O_2^-\cdot$ and preventing the recombination of e^- and h^+.[52] So the absence of oxygen in N_2-saturated suspension results in more suppression of degradation efficiency than the addition of

BQ due to the double negative effect. The addition of TBA causes a relatively weaker inhibition with degradation efficiency reduced by 17.9%, indicating that ·OH is also involved in the photocatalytic reaction although not the most important one. The generation of active radicals of O_2^-· and ·OH is further confirmed by ESR with DMPO technique. As shown in Fig. 10b, the characteristic peaks of DMPO-O_2^-· adducts is gradually observed in methanol dispersion under simulated sunlight irradiation and no such signal is detected in dark. Similarly, the DMPO-·OH adducts are also detected in aqueous dispersion of BOC clusters under irradiation, in which the featured peaks are the same as that reported in Ref.[53] The ESR results suggest that the simulated solar irradiation is essential to the generation of O_2^-· and ·OH radicals. The above scavenger and ESR experiments demonstrate that h^+, O_2^-· and ·OH together contribute to the photocatalytic oxidation of RhB molecules over BOC clusters.

According to previous analysis, RhB molecules are decomposed by minor photosensitization and dominant photocatalysis, in which the oxidative species has been ascertained. Combined the band edges of BOC semiconductor, the redox potential of active species, and the ground-excited state potential of RhB, a proposed migration mechanism of the photogenerated carriers on the surface of BOC cluster is illustrated in Fig. 11. Under the simulated sunlight irradiation, the electron of RhB adsorbed on the surface of BOC is excited from ground state into excited state. Forced by the potential difference of RhB* (-1.42 V *vs.* NHE)[54] and the conduction band (CB) position of BOC (-0.76 V *vs.* NHE),[55] the excited electron is injected from RhB to the

CB of BOC, leaving RhB[*] to be degraded through indirect photosensitization. In fact, the degradation of RhB is mainly achieved *via* photocatalysis under the strong oxidation of active holes and free radicals. As indicated in Fig. 11, the BOC can also be excited by simulated sunlight irradiation to generate CB electrons and valence band (VB) holes, which would rapidly migrate to the surface of photocatalyst and participate in the photocatalytic process. The VB potential of BOC is calculated to be 2.47 V based on the CB positon and the estimated E_g of 3.23 eV from the DRS spectrum. The strong oxidation ability enables the holes to directly oxidize RhB as the most important active species, which has been affirmed with EDTA scavenger. In addition, the hole can also oxidize OH^{-} or H_2O in RhB aqueous solution to form ·OH due to the slightly anodic VB position compared with the redox potential of ·OH/OH^{-} (2.38 V *vs.* NHE).[56] While the CB electrons are captured by the adsorbed molecular oxygen to yield O_2^-· in view of the more cathodic CB postion of -0.76 V compared with the redox potential of O_2/O_2^-· (-0.28 V *vs.* NHE).[57] Then the reactive species of holes, O_2^-· and ·OH as well as little photosensitization together result in the degradation and mineralization of organic molecules.

4. Conclusions

In summary, the {001} facets predominated $Bi_2O_2CO_3$ clusters were successfully synthesized through a mild hydrothermal method at 60 °C by fine-tuning the Na_2CO_3 dosage and reaction temperature. The sample exhibits obviously higher photocatalytic activities and excellent circulating stability for degradation of organic dyes than BOC plates with less exposed {001} planes. The reactive high energy {001} facets with

faster charge migration ability make a major contribution for the enhanced photocatalytic behavior. And the higher BET surface area of BOC clusters is a minor factor due to the slight increased adsorption to dye. The work provides a better understanding of the correlations among preparation parameter, specific structure and photocatalytic performance of the BOC photocatalyst. The holes, superoxide radicals and hydroxide radicals are ascertained to be oxidative species in the photocatalytic process over BOC clusters.

Acknowledgements

References

1   X. Chen, S. Shen, L. Guo and S. S. Mao, *Chem. Rev.*, 2010, **110,** 6503-6570.

2   H. Tong, S. X. Ouyang, Y. P. Bi, N. Umezawa, M. Oshikiri and J. H. Ye, *Adv. Mater.*, 2012, **24,** 229-251.

3   A. Fujishima and K. Honda, *Nature*, 1972, **238,** 37-38.

4   K. Maeda, T. Takata, M. Hara, N. Saito, Y. Inoue, H. Kobayashi and K. Domen, *J. Am. Chem. Soc.*, 2005, **127,** 8286-8287.

5   W. Luo, Z. Yang, Z. Li, J. Zhang, J. Liu, Z. Zhao, Z. Wang, S. Yan, T. Yu and Z. Zou, *Energy Environ. Sci.*, 2011, **4,** 4046-4051.

6   S. Pal, S. Maiti, U. N. Maiti and K. K. Chattopadhyay, *CrystEngComm*, 2015, **17,**

1464-1476.

7　X. F Shi, X. Y. Xia, G. W. Cui, N. Deng, Y. Q. Zhao, L. H. Zhuo and Bo Tang, *Appl. Catal. B*, 2015, **163**, 123-128.

8　S. Gong, Q. F. Han, X. Wang and J. W. Zhu, *CrystEngComm.*, 2013, **15**, 9185-9192.

9　F. Amano, A. Yamakata, K. Nogami, M. Osawa and B. Ohtani, *J. Am. Chem. Soc.*, 2008, **130**, 17650-17651.

10　M. Zhang, C. Shao, P. Zhang, C. Su, X. Zhang, P. Liang, Y. Sun and Y. Liu, *J. Hazard. Mater.*, 2012, **225-226**, 155-163.

11　D. Tang, H. C. Zhang, H. Huang, R. H. Liu, Y. Z. Han, Y. Liu, C. Y. Tong and Z. H. Kang, *Dalton Trans.*, 2013, **42**, 6285-6289.

12　Y. Peng, D. Wang, H. Y. Zhou and A. W. Xu, *CrystEngComm.*, 2015, **17**, 3845-3851.

13　J. Xiong, Q. Dong, T. Wang, Z. Jiao, G. Lu and Y. Bi, *RSC Adv.*, 2014, **4,** 583-586.

14　R. Hao, X. Xiao, X. Zuo, J. M. Nan and W. D. Zhang, *J. Hazard. Mater.*, 2012, **209-210,** 137-145.

15　H. W. Huang, X. Han, X. W. Li, S. C. Wang, P. K. Chu and Y. H. Zhang, *ACS Appl. Mater. Interfaces*, 2015, **7**, 482-492.

16　H. W. Huang, Y. He, Z. S. Lin, L. Kang and Y. H. Zhang, *J. Phys. Chem. C*, 2013, **117**, 22986-22994.

17　J.D. Grice, *Can. Mineral.*, 2002, **40,** 693-698.

18   R. Chen, M. H. So, J. Yang, F. Deng and H. Z. Sun, *Chem. Commun.*, 2006, **21,** 2265-2267.

19   X.Y. Chen, H.S. Huh and S.W. Lee, *J. Solid State Chem.*, 2007, **180,** 2510–2516.

20   Y. Y. Liu, Z. Y. Wang, B. B. Huang, K. S. Yang, X. Y. Zhang, X. Y. Qin and Y. Dai, *Appl. Surf. Sci.*, 2010, **257,** 172-175.

21   X. P. Lin, T. Huang, F. Q. Huang, W. D. Wang and J. L. Shi, *J. Phys. Chem. B*, 2006, **110,** 24629-24634.

22   H. F. Cheng, B. B. Huang, K. S. Yang, Z. Y. Wang, X. Y. Qin, X. Y. Zhang and Y. Dai, *Chem. Phys. Chem.*, 2010, **11,** 2167-2173.

23   T. Y. Zhao, J. T. Zai, M. Xu, Q. Zou, Y. Z. Su, K. X. Wang and X. F. Qian, *CrystEngComm.*, 2011, **13,** 4010-4017.

24   H. Y. Liang, Y. X. Yang, J.C. Tang and M. Ge, *Mat. Sci. Semicon. Proc.*, 2013, **16,** 1650-1654

25   F. Dong, Y. J. Sun, M. Fu, W. K. Ho, S. C. Lee and Z. B. Wu, *Langmuir*, 2012, **28,** 766-773.

26   Z. Y. Zhou, N. Tian, J. T. Li, I. Broadwell and S. G. Sun, *Chem. Soc. Rev.*, 2011, **40,** 4167-4185.

27   S. He, S. Zhang, J. Lu, Y. Zhao, J. Ma, M. Wei, D. G. Evans and X. Duan, *Chem. Commun.*, 2011, **47,** 10797-10799.

28   H. G. Yang, C. H. Sun, S. Z. Qiao, J. Zou, G. Liu, S. C. Smith, H. M. Cheng and G. Q. Lu, *Nature*, 2008, **453,** 638-641.

29   G. Liu, H. G. Yang, X. Wang, L. Cheng, J. Pan, G. Q. Lu and H. M. Cheng, *J. Am.*

Chem. Soc., 2009, **131,** 12868-12869.

30 J. Jiang, K. Zhao, X. Y. Xiao and L. Z. Zhang, *J. Am. Chem. Soc.*, 2012, **134,** 4473-4476.

31 Y. Xu, S. C. Xu, S. Wang, Y. X. Zhang and G. H. Li, *Dalton Trans.*, 2014, **43,** 479-485.

32 L. M. Yang, G. Y. Zhang, Y. Liu, Y. Y. Xu, C. M. Liu and J. W. Liu, *RSC Adv.*, 2015, **5,** 79715-79723.

33 H. W. Huang. Y. He, X. W. Li, M. Li, C. Zeng, F. Dong, X. Du, T. R. Zhang and Y. H. Zhang, J. Mater. Chem. A, 2015, **3**, 24547-2455**6.**

34 Y. Zheng, F. Duan, M. Q. Chen and Y. Xie, *J. Mol. Catal. A: Chem.*, 2010, **317,** 34-40.

35 H. W. Huang, J. J. Wang, F. Dong, Y. X. Guo, N. Tian, Y. H. Zhang and T. R. Zhang, *Cryst. Growth Des.* 2015, **15,** 534-537.

36 L. Chen, R. Huang, S. F. Yin, S. L. Luo and C. T. Au, *Chem. Eng. J.,* 2012, **193-194**, 123-130.

37 Y. Zhou, H. Y. Wang, M. Sheng, Q. Zhang, Z. Y. Zhao, Y. H. Lin, H. F. Liu and G. R. Patzke, *Sens. Actuators B,* 2013, **188**, 1312-1318.

38 A. P. Zhang and J. Z. Zhang, *J. Hazard. Mater.*, 2010, **173,** 265-272.

39 H. Z. Wang, Z. B. Wu and Y. Liu, *J. Phys. Chem. C*, 2009, **113,** 13317-13324.

40 A. Purkayastha, Q. Y. Yan, M. S. Raghuveer, D. D. Gandhi, H. F. Li, Z. W. Liu, R. V. Ramanujan, T. Borca-Tasciuc and G. Ramanath, *Adv. Mater.*, 2008, **20,** 2679-2684.

41 S. Shamaila, A. K. L. Sajjad, F. Chen and J. L. Zhang, *Appl. Catal., B*, 2010, **94,** 272-280.

42 F. Dong, S.C. Lee, Z. B. Wu, Y. Huang, M. Fu, W. K. Ho, S. C. Zou and B. Wang, *J. Hazard. Mater.*, 2011, **195,** 346-354.

43 A. N. Christensen, M. A. Chevallier, J. Skibsted and B. B. Iversen, *J. Chem. Soc., Dalton Trans.*, 2000, 265-270.

44 S. Brunauer, L. S. Deming, W. S. Deming and E. Teller, *J. Am. Chem. Soc.*, 1940, **62,** 1723-1732.

45 Z. H. Ai, W. K. Ho, S. C. Lee and L. Z. Zhang, *Environ. Sci. Technol.*, 2009, **43,** 4143-4150.

46 Y. Ohko, K. Hashimoto and A. Fujishima, *J. Phys. Chem. A*, 1997, 101, 8057-8062.

47 F. Chen, J. Zhao and H. Hidaka, *Int. J. Photoenergy,* 2003, **5,** 209-217.

48 K. Fujihara, S. Izumi, T. Ohno and M. Matsumura, *J. Photochem. Photobiol., A*, 2009, **132,** 99-104.

49 H. W. Huang, X. W. Li, J. J. Wang, F. Dong, P. K. Chu, T. R. Zhang and Y. H. Zhang, *ACS Catal.*, 2015, **5,** 4094-4103.

50 H. J. Lu, L. L. Xu, B. Wei, M. Y. Zhang, H. Gao and W. J. Sun, *Appl. Surf. Sci.*, 2014, **303,** 360-366.

51 M. Ge, N. Zhu, Y. P. Zhao, J. Li and L. Liu, *Ind. Eng. Chem. Res.*, 2012, **51,** 5167-5173.

52 Z. J. Zhang, W. Z. Wang, E. P. Gao, M. Shang and J. H. Xu, *J. Hazard. Mater.*,

2011, **196,** 255-262.

53   S. Zhang, S. J. Zhang and L. M. Song, *Appl. Catal., B*, 2014, **152–153,** 129-139.

54   J. L. Hu, W. J. Fan, W. Q. Ye, C. J. Huang and X. Q. Qiu, *Appl. Catal., B*, 2014, **158−159,** 182-189.

55   Z. Y. Zhao, Y. Zhou, F. Wang, K. H. Zhang, S. Yu and K. Cao, *ACS Appl. Mater. Interfaces,* 2015, **7,** 730-737.

56   Y. Y. Liu, Z. Y. Wang, B. B. Huang, X. Y. Zhang, X. Y. Qin and Y. Dai, *J. Colloid Interface Sci.*, 2010, **348,** 211-215.

57   Y. L. Zhang, D. Y. Li, Y. G. Zhang, X. F. Zhou, S. J. Guo and L. B. Yang, *J. Mater. Chem. A*, 2014, **2,** 8273-8280.

Figures and captions
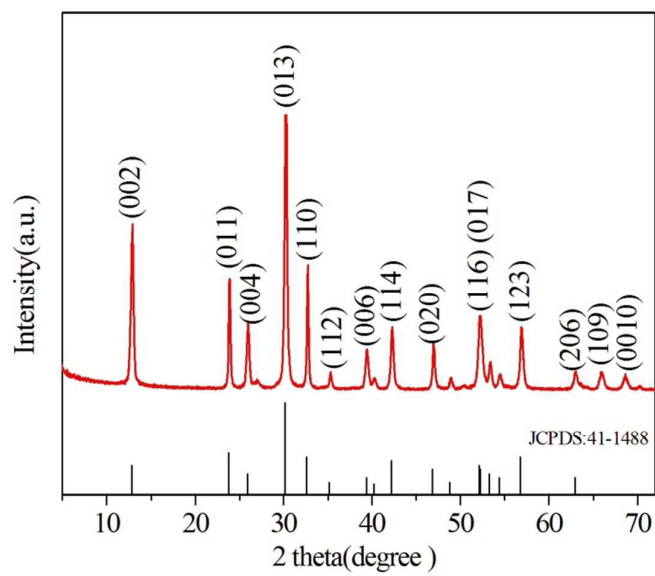
Fig.1 XRD pattern of the as-synthesized BOC sample (The JCPDS standard is at the

bottom).
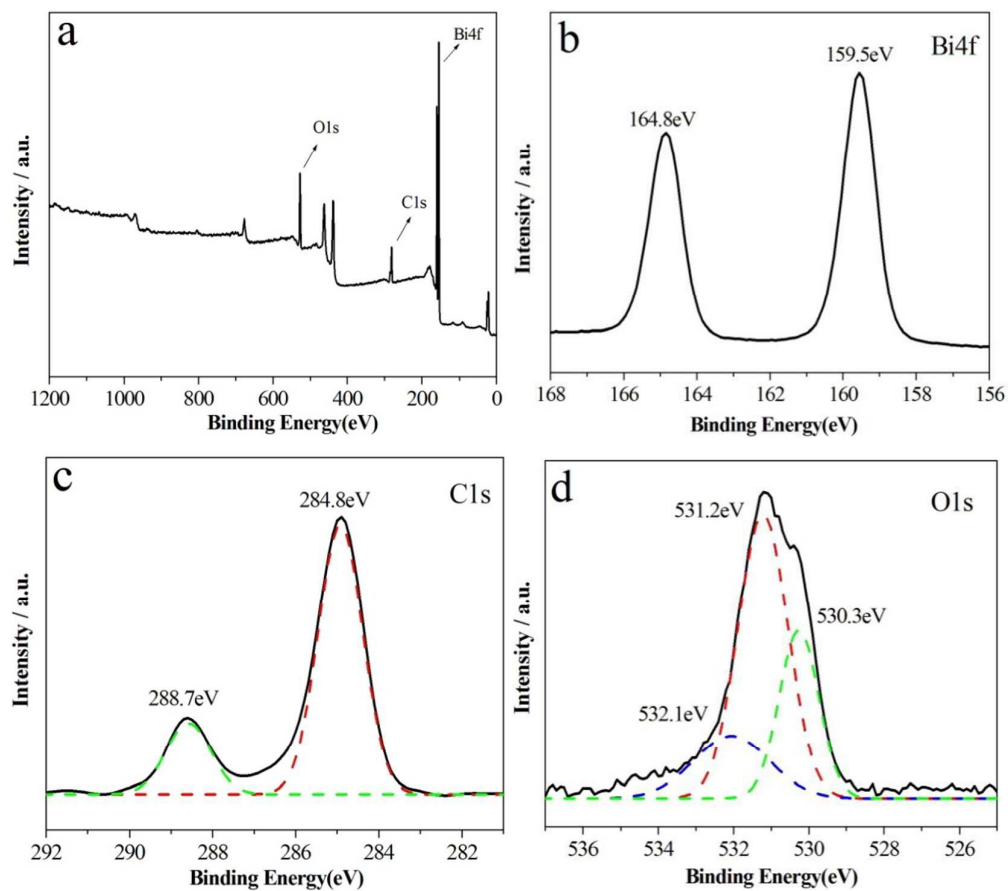
Fig.2 XPS spectra of the BOC sample: (a) the survey spectrum, (b-d) the high

resolution of Bi4f, C1s and O1s, respectively.
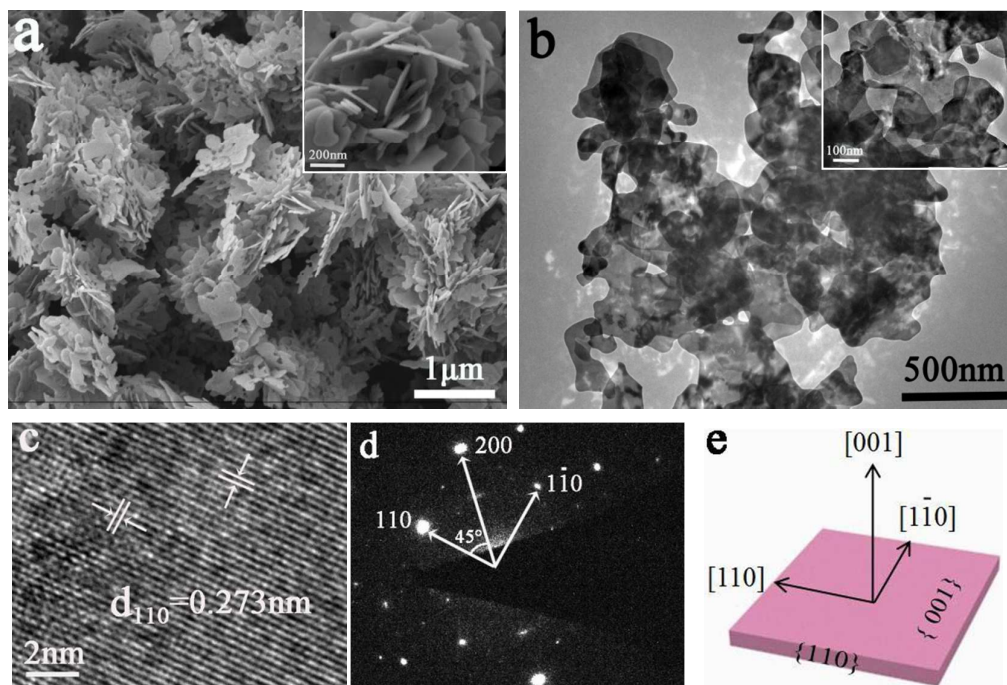
Fig. 3 Morphology and microstructure of BOC sample: (a) SEM image, (b) TEM image, (c) HRTEM image, (d) SAED pattern, and (e) schematic orientation of building units .
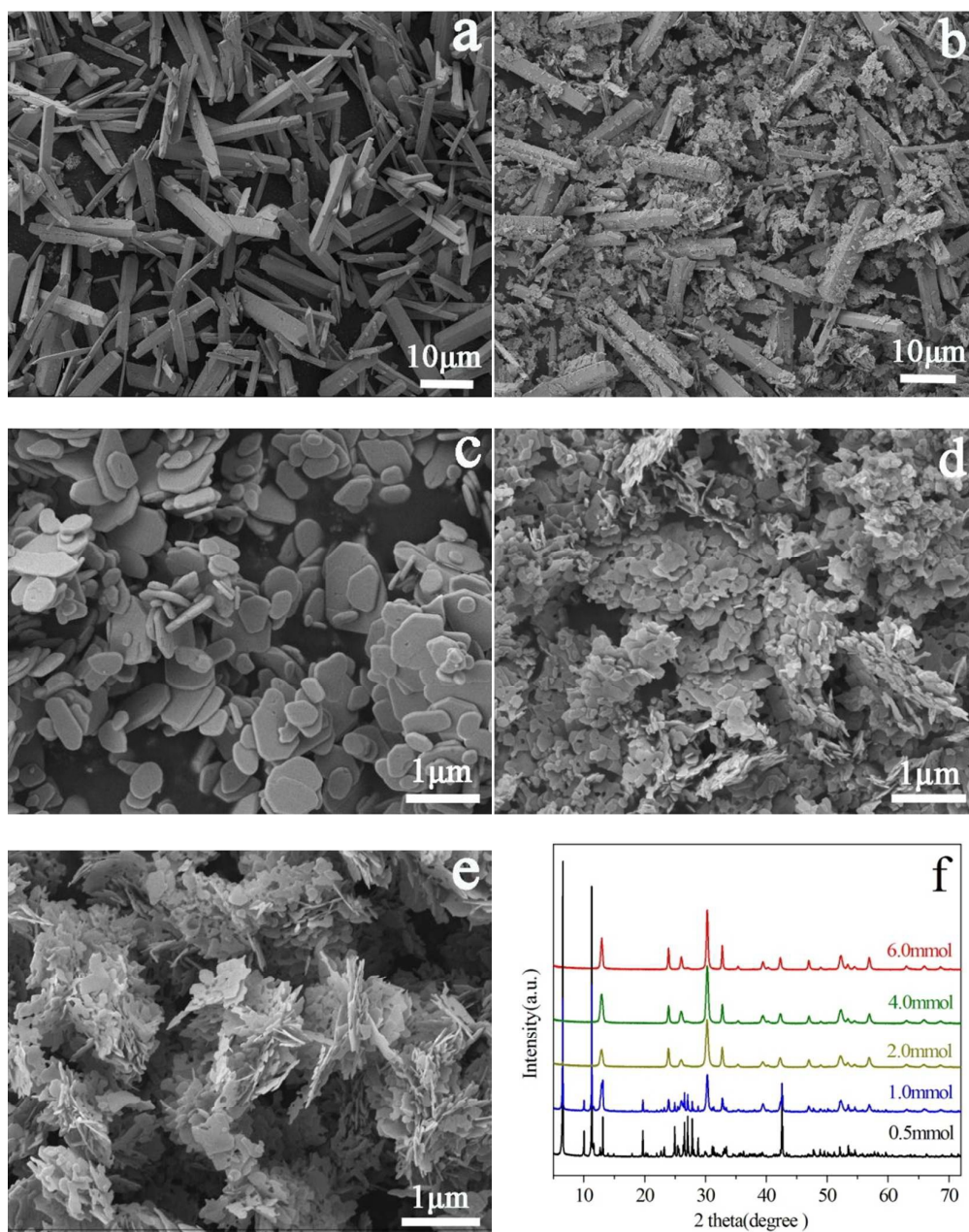
Fig. 4 SEM images and XRD patterns of the Na_2CO_3 dosage series samples: (a) 0.5 mmol, (b) 1.0 mmol, (c) 2.0 mmol, (d) 4.0 mmol, (e) 6.0mmol, and (f) corresponding XRD patterns.
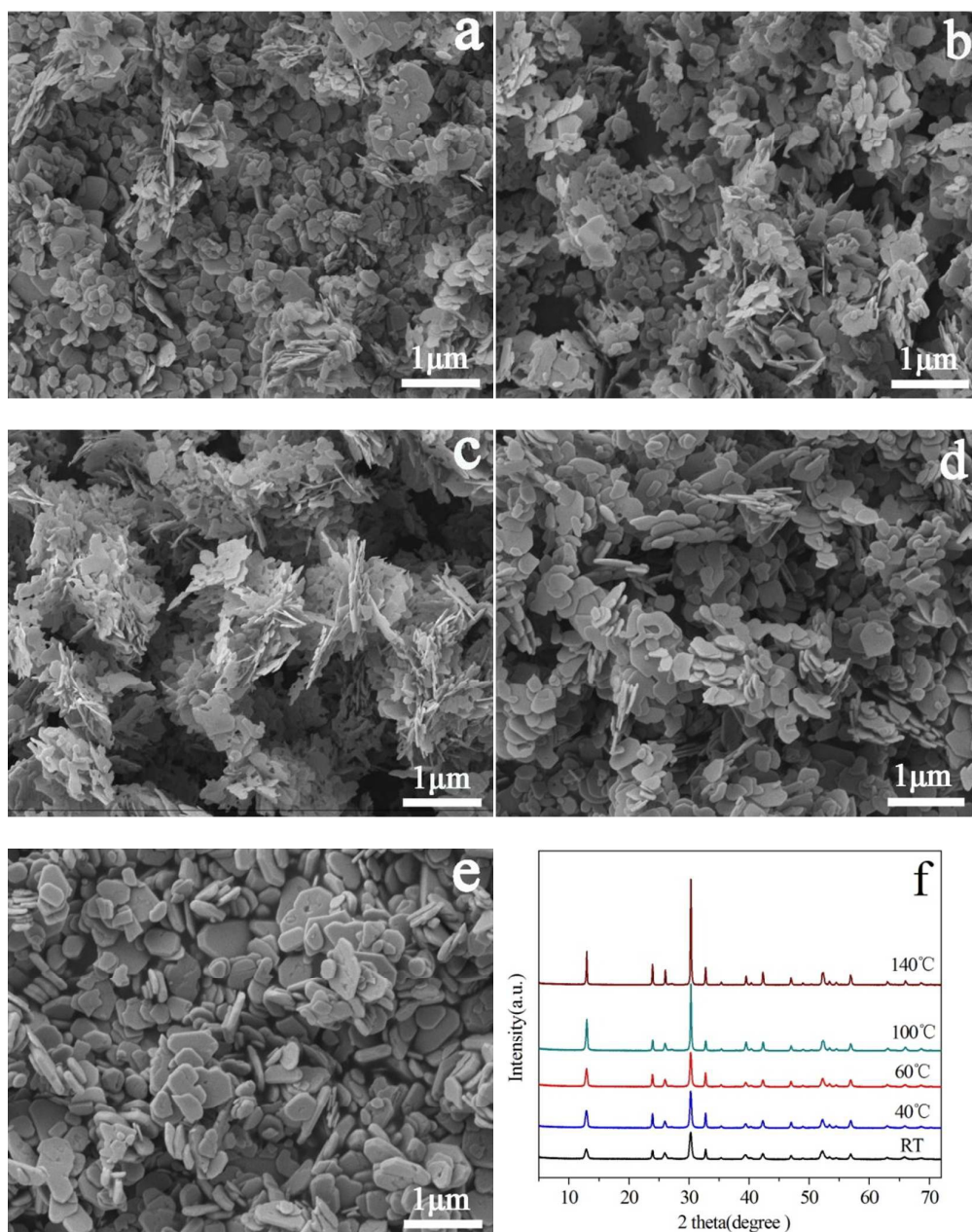
Fig. 5 SEM images and XRD patterns of the temperature series samples: (a) ambient temperature (RT), (b) 40 °C, (c) 60 °C, (d) 100 °C, (e) 140 °C, and (f) corresponding XRD patterns.
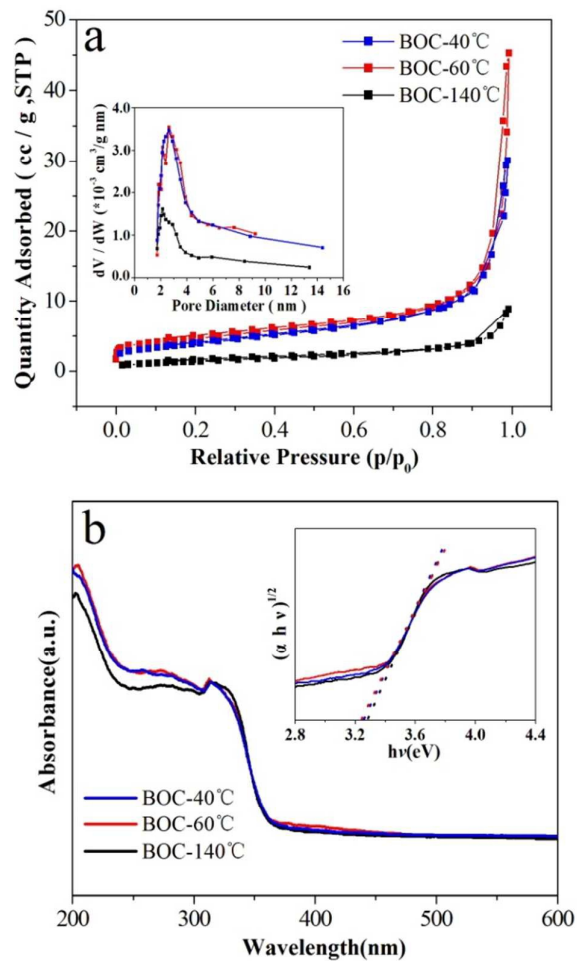
Fig. 6 (a) N_2 sorption isotherm with BJH pore-size distribution plot in inset and (b)

DRS spectra of **BOC samples obtained at 40 °C, 60 °C and 140 °C**, respectively.
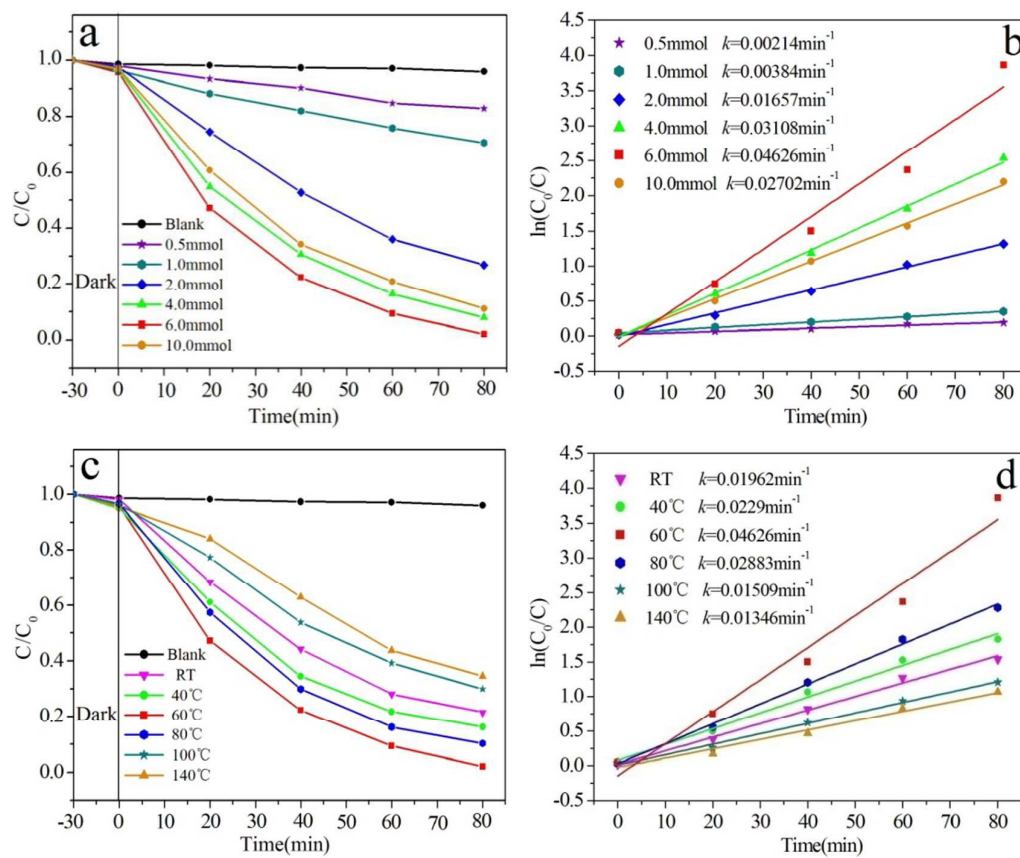
Fig. 7 Photocatalytic degradation of RhB and corresponding pseudo first-order plots

over samples of (a, b) Na$_2$CO$_3$ dosage series, and (c, d) temperature series.
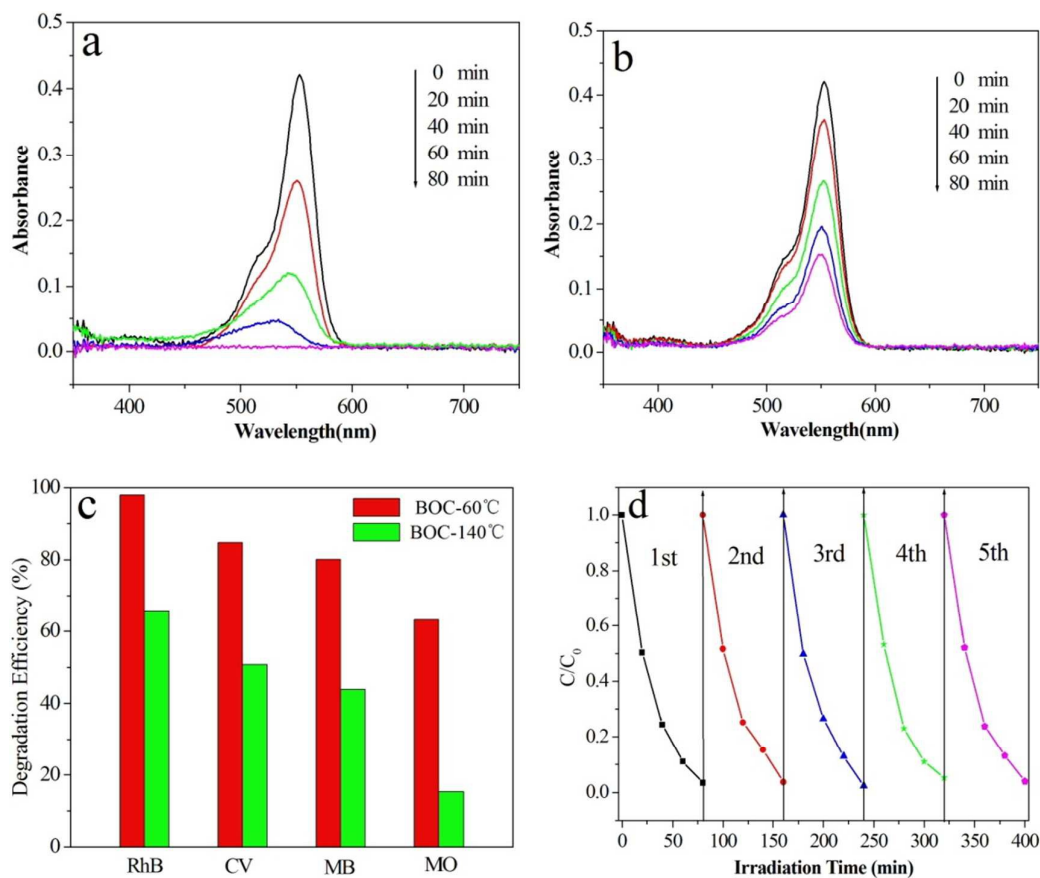
Fig. 8 (a, b) temporal evolution of RhB absorption spectra over BOC-60°C and BOC-140°C, respectively, (c) comparison of photodegradation for different dyes, and (d) reuse of BOC-60°C.
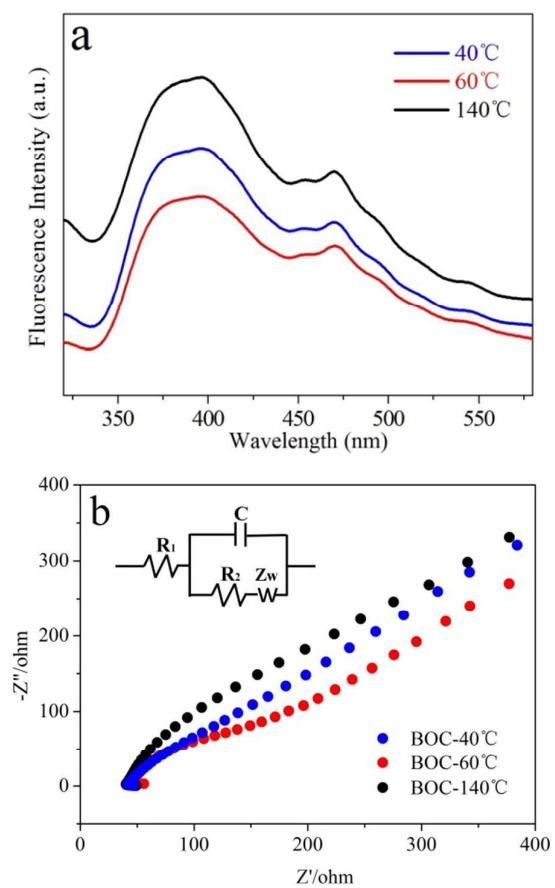
Fig. 9 (a) PL spectra and (b) EIS Niquist plots of BOC samples obtained at **40°C**, 60°C and 140°C **with fitted equivalent circuit**, respectively.
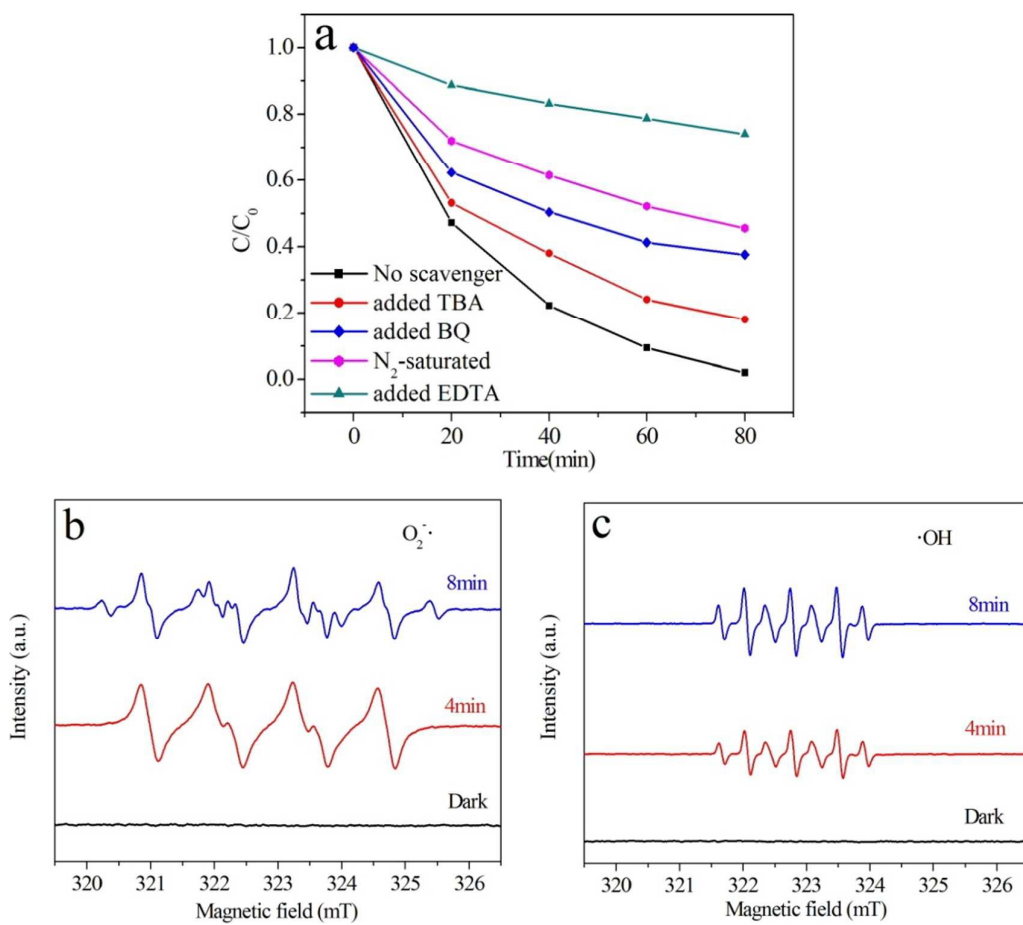
Fig. 10 (a) Reactive species trapping experiments of BOC clusters; ESR spectra of radical adducts trapped by DMPO in BOC-60°C methanol (b) and aqueous (c) dispersions, respectively.
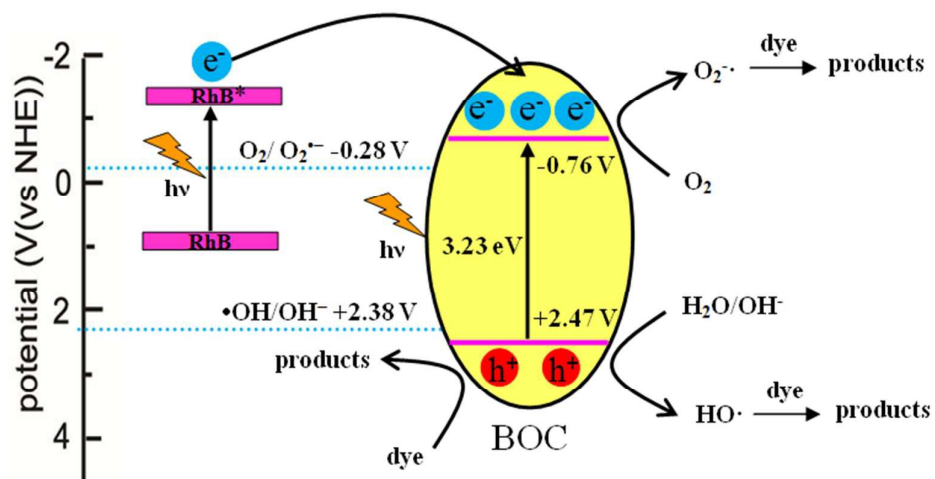
Fig. 11 Schematic illustration of the charge separation and migration on the surface of

BOC clusters.